MDPI

Article

On-Site Application of Solar-Activated Membrane (Cr–Mn-Doped TiO$_2$@Graphene Oxide) for the Rapid Degradation of Toxic Textile Effluents

Maryam Yousaf [1], Mariam Akram [2], Ijaz Ahmad Bhatti [2], Muhammad Ahmad [1,*], Muhammad Usman [3,*], Muhammad Usman Khan [4], Abid Sarwar [5], Muhammad Sultan [6] and Ihsanullah Sohoo [7]

1 School of Chemistry and Chemical Engineering, Beijing Institute of Technology, Beijing 102488, China
2 Department of Chemistry, University of Agriculture Faisalabad, Faisalabad 38040, Pakistan
3 Institute for Water Resources and Water Supply, School of Civil Engineering, Hamburg University of Technology, Am Schwarzenberg-Campus 1, 21073 Hamburg, Germany
4 Department of Energy Systems Engineering, Faculty of Agricultural Engineering and Technology, University of Agriculture Faisalabad, Faisalabad 38000, Pakistan
5 Department of Irrigation & Drainage, University of Agriculture Faisalabad, Faisalabad 38000, Pakistan
6 Department of Agricultural Engineering, Bahauddin Zakariya University, Multan 60800, Pakistan
7 Department of Energy and Environment Engineering, Dawood University of Engineering and Technology, New M.A. Jinnah Road, Karachi 74800, Pakistan
* Correspondence: muhammadahmad@pku.edu.cn (M.A.); muhammad.usman@daad-alumni.de (M.U.)

Abstract: Solar-activated water treatment has become an emerging research field due to its eco-friendly nature and the economic feasibility of green photocatalysis. Herein, we synthesized promising, cost-effective, and ultralong-semiconductor TiO$_2$ nanowires (NW), with the aim to degrade toxic azo dyes. The band gap of TiO$_2$ NW was tuned through transition metals, i.e., chromium (Cr) and manganese (Mn), and narrowed by conjugation with high surface area graphene oxide (GO) sheets. Cr–Mn-doped TiO$_2$ NWs were chemically grafted onto GO nanosheets and polymerized with sodium alginate to form a mesh network with an excellent band gap (2.6 eV), making it most suitable to act as a solar photocatalytic membrane. Cr–Mn-doped TiO$_2$ NW @GO aerogels possess high purity and crystallinity confirmed by Energy Dispersive X-ray spectroscopy and X-ray diffraction pattern. A Cr–Mn-doped TiO$_2$ NW @GO aerogels membrane was tested for the photodegradation of Acid Black 1 (AB 1) dye. The synthesized photocatalytic membrane in the solar photocatalytic reactor at conditions optimized by response surface methodology (statistical model) and upon exposure to solar radiation (within 180 min) degraded 100% (1.44 kg/m^3/day) AB 1dye into simpler hydrocarbons, confirmed by the disappearance of dye color and Fourier transform infrared spectroscopy. An 80% reduction in water quality parameters defines Cr–Mn-doped TiO$_2$ NW @GO aerogels as a potential photocatalytic membrane to degrade highly toxic pollutants.

Keywords: photocatalysis; graphene oxide; dye degradation; solar-activated membrane; TiO$_2$ nanowire

1. Introduction

Water contamination is a major problem faced by the entire world, especially in developing countries. According to a rough estimation, around four billion people throughout the world have no or very little supply of clean water, and yearly, millions of people died due to drinking contaminated water [1–3]. Many industries, such as paper, pulp, dyestuff, pharmaceutical textiles, etc., are running throughout the world [4–6]. A huge number of pollutants are being discharged from these industrial processes that cause noticeable effects on the environment [7]. Around 20% of colored waste effluents are being discharged into water bodies from textile industries without treatment, which is badly polluting the environment. These colored effluents are rich in organic dye pollutants, and because of the non-biodegradable nature of these contaminants, they are a serious environmental risk

and continuously disturb human life [8,9]. These organic dyes are not only aesthetically displeasing but also disturb the visual quality of water, which hinders light penetration. Moreover, dyes present in water reduce dissolved oxygen, ultimately affecting aquatic life. Humans, upon consuming this water contaminated with dyes, suffer from several diseases such as cancer, heart problems, respiratory diseases, diarrhea, jaundice (hepatitis), etc. Therefore, removing these dyes from the water before consumption is imperative to avoid health effects [10–12].

However, organic contaminants present in the industrial effluent are difficult to be removed by the natural degradation process owing to their biological and chemical stability [13,14]. So far, methods reported for the removal of organic dyes are ion exchange, adsorption, photocatalysis, chemical oxidation, coagulation, biodegradation, Fenton oxidation degradation, chemical reduction, and electrochemical treatment, etc. [15–17]. Unfortunately, the main drawbacks of these techniques are their low dye removal efficiencies, slow reaction rates, narrow operating pH range, the problem of the disposal of the spent contaminated activated sludge, and the control of the appropriate dye removal conditions [18–20]. Among these techniques, the removal of dyes from contaminated water using the advanced oxidation process (AOP), mainly photocatalysis, is considered to be the most efficient process. In recent years, substantial attention has been paid to the AOPs, which are characterized by the generation of a hydroxyl radical ($^\bullet$OH) by a nano-photocatalyst; nano-photocatalysts possess extraordinary properties due to the quantum confinement effect of nanomaterials [21–23]. The $^\bullet$OH produced during photocatalysis possesses a high oxidation potential (estimated to be +2.8 V) relative to other oxidants, which is why it can oxidize the organic dyes [24,25].

Mechanistically, photocatalysis is a photo-induced process, during which, electron and hole pairs are generated by photocatalysts upon exposure to light, which in turn generates highly reactive $^\bullet$OH radicals [26]. The photocatalytic efficiency of the photocatalyst can be enhanced by doping with metal and non-metal ions [27–29]. Different semiconductors oxides, such as TiO_2, ZnO, ZnS, and WO_3 have been used as photocatalysts [30,31]. Among the reported photocatalysts, TiO_2, due to its strong oxidizing power, photostability high surface-to-volume ratio, and low toxicity, is considered a suitable candidate to be used as a photocatalyst. However, its wide band gap of 3.0–3.2 eV, UV light absorption capacity, and transparency to visible light restrict its broader application [32]. The crystalline structure of TiO_2 has been modified by doping with metals (Fe, Zn, Cu, Ni, Cd, V) and non-metals (N, C) [33], lanthanides (Eu, Gd, La, Yb) [34], and noble metals (Ag, Pt, Au) to reduce its band gap energy suitable for visible light absorption [35–37]. The TiO_2 band gap is modified by the crystalline modification by replacing the Ti atoms in the TiO_2 crystal lattice by doping with different metals and non-metals with different charge/oxidation states, and the stability of the newly formed doped TiO_2 is dependent upon the crystallite size [34]. Crystalline TiO_2 can be prepared by the hydrothermal method, the extraction–pyrolytic method, and the precipitation method with variable properties [38,39].

However, compared to high-cost noble metals, the low cost and superior properties of transition metals show promise for doping and altering the electronic properties of TiO_2 [40]. Another problem faced in photocatalysis is the rapid electron–hole pair recombination; this problem in TiO_2 after band gap tuning can be overcome by conjugating with graphene oxide (GO). GO/TiO_2 acts as a photocatalyst by efficiently degrading dye like Acid Black under UV and visible irradiation. The large surface area and oxygen-containing functional groups of GO facilitate the adsorption of dye on photocatalysts with high quantum efficiency to resist the recombination of the electron pair [41,42]. This conjugated mixture can be turned into a polymeric photocatalytic membrane by means of combining it with sodium alginate polymer in the form of aerogels. Aerogel has very unique properties such as its low density, high surface area, and porosity [43,44].

Keeping these facts in consideration, herein, the band gap of TiO_2 was tuned by doping with the transition metals, i.e., chromium (Cr) and manganese (Mn). Cr and Mn exist in variable oxidation/charge states that can create an electron transport chain, facilitating the

more feasible redox photocatalytic degradation process of dyes [37]. After co-doping with Cr–Mn, TiO$_2$ was conjugated with GO to form a Cr–Mn-doped TiO$_2$@GO composite that was polymerized into aerogel photocatalytic membrane for the solar-assisted photocatalytic degradation of Acid Black 1 dye. All operational parameters, i.e., oxidant concentration (H$_2$O$_2$), pH and sunlight exposure time, and the size of the aerogel to study the photo-degradation of Acid Black 1, were optimized by response surface methodology (RSM). Because of our synthesized Cr–Mn-doped TiO$_2$@GO aerogel photocatalytic membrane's large internal surface area, porosity, high optical properties, low density, and high adsorptive site due to GO functionalities, it favors the greater interaction of pollutants with the membrane leading to 100% degradation within 180 min of exposure to solar light. The employment of our designed photocatalytic membrane will be cost-effective because of the simultaneous adsorption and photodegradation of toxic organic pollutants [45–47].

2. Materials and Methods

2.1. Materials and Chemicals

Titanium oxide Anatase (TiO$_2$), chromium nitrate (Cr(NO$_3$)$_3$), manganese nitrate (Mn(NO$_3$)$_2$), sodium chloride (NaCl), sodium hydrogen phosphate (NaHPO$_4$), calcium chloride (CaCl$_2$), sodium alginate (Na alginate), citric acid, hydrogen peroxide (H$_2$O$_2$), sodium hydroxide (NaOH), and hydrochloric acid (HCl) were used, which were obtained from the Radiation Lab. All reagents used were of analytical grade and used further without any purification.

2.2. Synthesis of Graphene Oxide (GO) and TiO$_2$ Nanowire (NW)

Graphene oxide (GO) was synthesized by a bottom-up approach using the method reported in the literature with slight modification [48]. In brief, 2 g of citric acid (CA) was heated at 200 °C in heating in the mantle. Within 5 min of heating, the CA was liquified and changed color from white to pale yellow and finally turned to dark brown after three hours, indicating the formation of GO sheets. Later, the formed dark brown was removed from the mantel, cooled, and neutralized to pH 7 with 50 mL NaOH (0.1 M) solution. The resulting dark brown GO solution was stored for further use.

Cr–Mn-doped TiO$_2$ nanowires (NW) were prepared according to the previously reported literature [49]. In brief, the molten salt flux method was used for the synthesis of the Cr–Mn-doped TiO$_2$ NW. A total of 0.50 g of TiO$_2$ powder was mixed with the 2.0 g of NaCl and 0.50 g of NaHPO$_4$ in a 1:4:1 ratio, and 2.5% atomic percentage of Mn(NO$_3$)$_2$ and Cr(NO$_3$)$_3$ dopants. The whole reaction mixture was finely ground in a pestle mortar to form a fine powder mixture and then calcined in a crucible at the temperature of 825 °C for eight hours in a muffle furnace (ramping rate of 2 °C/min). After calcination, the prepared mixture was allowed to naturally cool down at room temperature, and then it was thoroughly washed with water to remove unreacted salts and dried in an oven at 80 °C for eight hours.

2.3. Synthesis of Cr–Mn-Doped TiO$_2$/Graphene Oxide Aerogels

Individually synthesized GO and Cr–Mn-doped TiO$_2$ NWs were used to prepare Cr–Mn-doped TiO$_2$ NW @GO aerogels using the polymerization method. In brief, 2.5 mL (0.2 g/100 mL) of GO was taken and diluted with 48.5 mL of distilled water followed by the addition of 0.5 g/50 mL of Na alginate (at 50 °C) and 0.16 g of Cr–Mn-doped TiO$_2$ NW; the whole reaction mixture was stirred for 20 min at room temperature to ensure polymerization. Later on, the gel was dropped into CaCl$_2$ solution (1.0 M) followed by freeze-drying for 4–5 h to obtain Cr–Mn-doped TiO$_2$ NW @GO aerogels.

2.4. Characterization of Cr–Mn-Doped TiO$_2$/Graphene Oxide Aerogels

The synthesized Cr–Mn-doped TiO$_2$ NW @GO aerogel was characterized through X-ray diffraction (XRD, Jeol JDX-3532 diffractometer, Tokyo, Japan) to study the crystal structure of the aerogel. Scanning Electron Microscopy (SEM, Quanta 250, FEG (Waltham,

MA, USA) analysis was conducted to determine the surface morphology. Energy Dispersive X-ray (EDX) analysis was performed to identify the elements present in the synthesized material. Fourier transform infrared spectroscopy (FTIR, Bruker IFS 125HR Japan, Tokyo, Japan) was conducted to identify the functional groups. The Brunauer–Emmett–Teller (BET) surface area and pore size analysis were performed by measuring the N_2 adsorption–desorption isotherms.

2.5. Statistical Analysis

The optimization of the operational reaction parameters, i.e., the size of the aerogels, irradiation time, pH, and oxidant concentration, was performed using Design Expert 7 pro software under Response Surface Methodology (RSM). RSM includes different designs, these designs are three-level factorial, central composite (CCD), Box–Behnken (BBD), and D-optimal [50]. Here, we used RSM in combination with central composite design (CCD) to optimize four operational reaction parameters; these parameters were chosen as independent variables while the degradation rate of the dye was chosen as the output response variable. The list of variables, and their actual lower and higher levels for optimization are given in Table 1. CCD design (CCD) was adopted to evaluate the combined effect of the four independent variables by 30 sets of experiments. A general expression of the mathematical relationship describing the response of four independent variables (A, B, C, D) can be approximated by quadratic polynomial Equation (1):

$$Y = \beta + \beta_1 X_1 + \beta_2 X_2 + \beta_3 X_3 + \beta_4 X_4 + \beta_{12} X_{12} + \beta_2 X_2 + \beta_{33} X_{32} + \beta_{44} X_{42} + \beta_{12} X_1 X_2$$
$$+ \beta_{13} X_1 X_3 + \beta_{14} X_1 X_4 + \beta_{23} X_2 X_3 + \beta_{24} X_2 X_4 + \beta_{34} X_3 X_4 \tag{1}$$

where Y presented the predicted response and β is the coefficient constant. While β_1, β_2, β_3, and β_4 are the linear effect coefficients, β_{11}, β_{22}, β_{33}, and β_{44} are the quadratic effect coefficients, and β_{12}, β_{13}, β_{14}, β_{23}, β_{24}, and β_{34} are the interaction effect coefficients. X1, X_2, X_3, and X_4 are the independent variables corresponding to A, B, C, and D, respectively.

Table 1. CCD with predictive values and their experimental results.

Factor	Variables	Unit	Low Actual	High Actual
A	pH		4	10
B	Oxidant concentration	mmol	10	50
C	Irradiation Time	min	60	300
D	Size of aerogels	mm	10	15

The data were analyzed by analysis of variance (ANOVA), and the mean values were considered of significant difference when $p < 0.0001$. The optimal values of the operational parameters were estimated by the three-dimensional response surface analysis of the independent variables and the dependent variable.
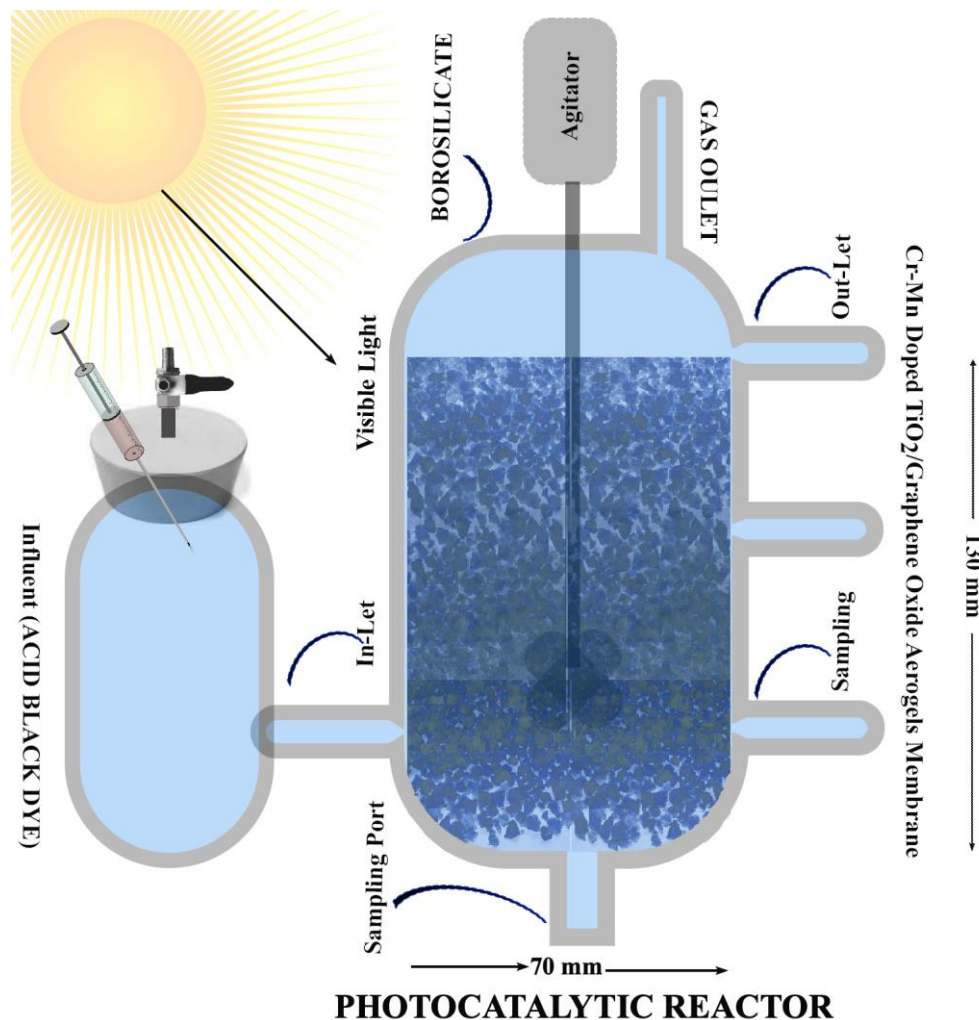
2.6. Photocatalytic Degradation Potential of Acid Black Dye by Cr–Mn-Doped TiO_2 NW @GO Aerogels

Solar light-assisted photocatalytic degradation of Acid Black 1 dye (AB 1) ($C_{36}H_{23}N_5Na_2O_6S_2$) by Cr–Mn-doped TiO_2 NW @GO aerogels photocatalyst was evaluated in borosilicate glass reactors (500 mL) filled with the Cr–Mn-doped TiO_2 NW @GO aerogel membrane (12.5 mm thickness). A reaction mixture containing a 500 ppm solution of AB 1 dye was exposed to solar radiation (one Sun illumination, wavelength = 530 nm) at conditions optimized by RSM in the solar photocatalytic reactor (Scheme 1). The rate of the degradation was measured with a UV–Vis spectrophotometer (Maximum wavelength = 620 nm) followed by the degradation % calculation using Equation (2):

$$(\text{Degradation (\%)}) = (A_0 - A_t)/(A_0) * 100 \tag{2}$$

where A_o: Absorbance of Dye at Zero minutes, A_t: Absorbance of Dye at time t.

The water quality parameters of the treated and untreated AB 1 dye-containing textile industrial effluents such as BOD, COD, and TOC were analyzed by using previously reported literature (Ahmad et al., 2019).

Scheme 1. Schematics of the photocatalytic reactor design and experimental setup for the degradation of AB 1 dye.

3. Results and Discussion

3.1. Characterization of Cr–Mn-Doped TiO2 NW @GO Aerogel

The crystal structure of the prepared Cr–Mn-doped TiO_2@GO aerogel was studied through XRD analysis (Figure 1a). The appearance of the XRD diffraction peaks at 2θ° values of 27.5°, (110), 36.04 (101), 41.31 (111), 54.28 (211), and 55.3° (102) confirmed the presence of the rutile phase of TiO_2 [51], while the absence of diffraction peaks corresponding to the oxides or metallic phase of Cr–Mn dopants confirmed the successful substitution of Cr–Mn with the Ti in the TiO_2 crystal structure. Furthermore, the poor crystalline nature of the dopant will favor enhanced oxygen vacancies and the catalytic nature of the Cr–Mn-doped TiO_2@GO aerogel. Moreover, the appearance of a diffraction peak at 2θ = 10.9° corresponded to the (100) plane of GO [52], confirming the presence of GO and the successful formation of the Cr–Mn-doped TiO_2 NW @GO aerogel.
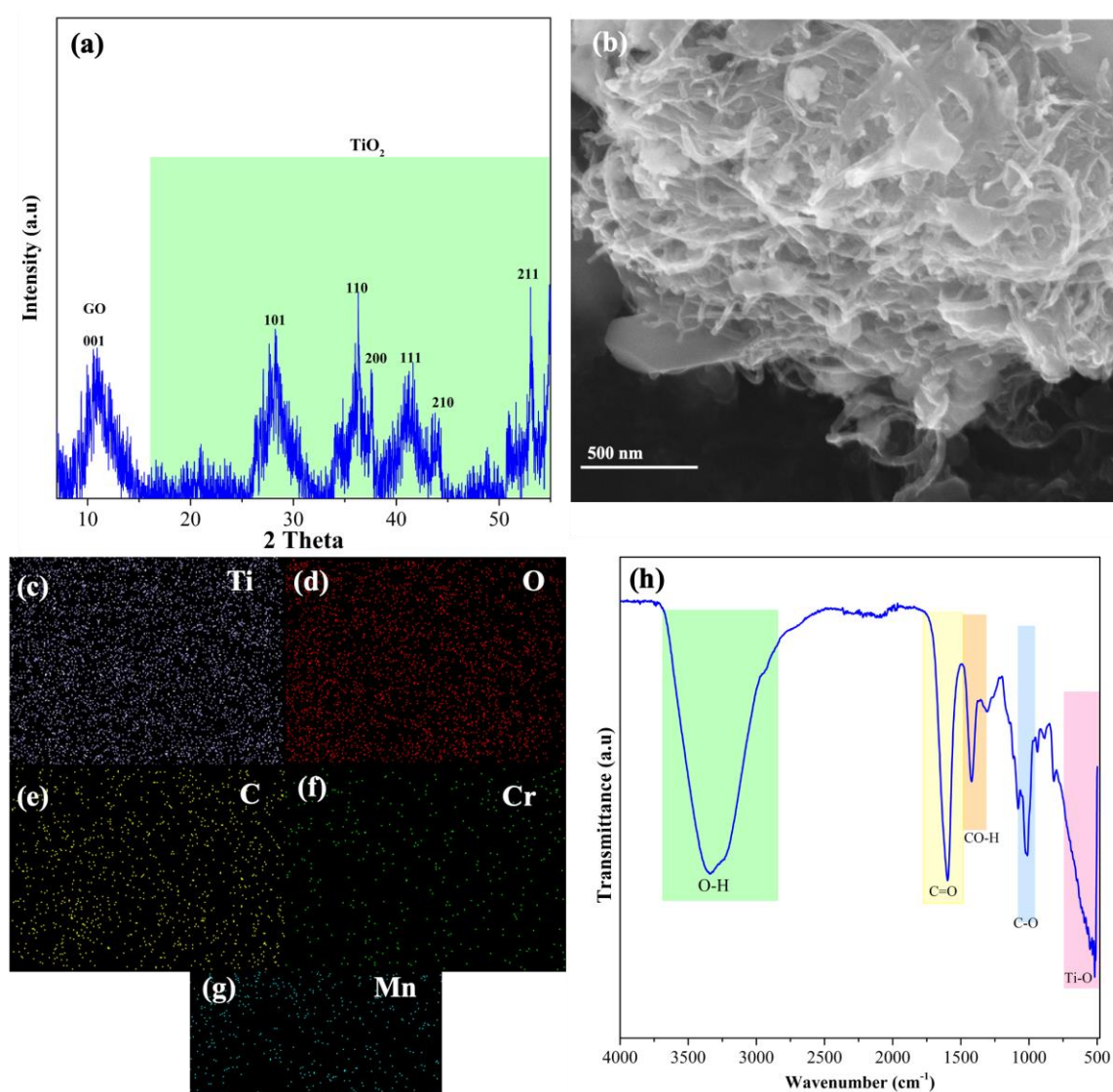
Figure 1. XRD crystallographic pattern (**a**), SEM micrograph (**b**), functional group analysis (**c–g**), and elemental analysis (**h**) of Cr–Mn-doped TiO_2@GO aerogel.

In order to analyze the structure and morphology of synthesized Cr–Mn-doped TiO_2@GO aerogel the SEM analysis was carried out (Figure 1b). A fine network of Cr–Mn-doped TiO_2 NWs surrounding the nanosheets of GO can be clearly seen in SEM images, which confirmed that Cr–Mn-doped TiO_2 NW is successfully grafted over GO nanosheets. During the polymerization process for the formation of aerogel, Cr–Mn-doped TiO_2 NWs completely attached to the surface of GO sheets which makes it difficult to differentiate between the Cr–Mn-doped TiO_2 NWs and the GO sheets. Further, the elemental analysis and purity of the Cr–Mn-doped TiO_2@GO aerogel were confirmed by EDX (Figure 1c–g). It is quite obvious from Figure 1c–f that the Ti, O, and C (a component of GO) in the prepared sample are present in higher concentrations, while Mn and Cr, being the dopants, are present in a lesser concentration in the EDX mapping. All these elements are the main components of the prepared Cr–Mn-doped TiO_2@GO aerogel.

The specific surface area (S_{BET}) and porosity of the prepared Cr–Mn-doped TiO_2@GO aerogel were evaluated with the help of N_2 adsorption–desorption isotherms through BET. From the results, it was obvious that the incorporation of Cr–Mn in TiO_2 enhanced its S_{BET} (79.3 m^2/g) compared to the pure TiO_2 (46.2 m^2/g). This enhancement is attributed to the control of the crystal grain size due to the incorporation of dopants. The surface area was further increased upon the addition of GO and the formation of an aerogel

structure (280.2 m^2/g). These results confirmed that the synthesized materials are highly porous in nature (Table 2). The high porosity of aerogel provides a microchannel for the efficient interaction of pollutants with the Cr–Mn-doped TiO$_2$@GO aerogel photocatalytic membrane. Moreover, the conjugation of Cr–Mn-doped TiO$_2$ NW with the GO nanosheets will not only enhance the surface area for pollutant interaction but also facilitate the photo-generated electron–hole separation and their transmission between the GO nanosheets and Cr–Mn-doped TiO$_2$ NW.

Table 2. BET-specific surface area and pore size of Cr–Mn-doped TiO$_2$ NW @GO aerogel.

Sr. No		TiO$_2$ NW	Cr–Mn-Doped TiO$_2$ NW	Cr–Mn-Doped TiO$_2$ NW @GO Aerogel
1	S$_{BET}$ (m^2/g)	46.2	79.3	280.2
2	Pore volume (cm^3/g)	0.135	0.216	0.35

FTIR analysis of Cr–Mn-doped TiO$_2$@GO aerogel shows (Figure 1d) the prominent broad peak from 500–1000 cm^{-1} corresponding to the Metal–O/Ti–O bonds in the crystal lattice and with the C of GO (Ti–O–C). A broad absorption peak at 3340 cm^{-1} was due to the stretching vibration of the O–H (hydroxyl) group of water molecules, which indicated the existence of water molecules. Additionally, the presence and conjugation of GO in the Cr–Mn-doped TiO$_2$@GO aerogel is confirmed from the characteristic stretching vibration peaks at 1030 cm^{-1} (epoxy C–O), 1425 cm^{-1} (C–OH) and 1570 cm^{-1} (ketone or carboxylate C=O) [53]. These hydroxyl and other oxygenated functional groups present at the corners and on the basal planes of GO could form bonds with the Ti–O and with functional groups of alginate to form a robust Cr–Mn-doped TiO$_2$@GO aerogel matrix.

3.2. Statistical Evaluation of Photo Catalytic Activity of Cr–Mn-Doped TiO$_2$@GO Aerogel

The RSM was utilized to optimize the conditions for the rapid photodegradation of AB 1 dye. Three-dimensional response surfaces were generated by using the Design Expert 7 pro software, which presented the visual relationship between different variables [54,55]. The RSM results of 30 runs were obtained on the basis of polynomial Equations (1) and (3) and are provided in Table 3.

$$\text{(Y)} = +85.00 + 4.82\,A + 6.17\,B + 0.60\,C - 1.55\,D - 4.76\,A\,B + 4.59\,A\,C + 1.62\,A\,D - 4.03\,B\,C - 1.01\,B\,D + 3.84\,C\,D - 11.53\,A2 - 7.53\,B^2 - 7.28\,C2 - 4.98\,D2 \tag{3}$$

where 'Y' is the degradation (%), and the actual values of the variables A, B, and C are shown in the equation. The validated model shows the interactive effects of variables on the degradation % (Y) of AB 1 dye under sunlight radiation. The interaction of parameters is demonstrated by the AB, AC, and BC processes. The parameters were related by coefficients and the signs (+, −) in the model. The coefficients indicate the specific weight of the parameters in the model, while the signs (+) and (−) affect the synergistic and antagonistic effects of variables on the response (Y). The coefficients indicated the weight of the variables in the model, which determines the important roles of the parameters in the AB 1 dye degradation.

According to the ANOVA, the *p*-value was less than 0.0001, which means that the model was significant; on the other hand, the *p*-value greater than 0.1000 showed that the model was not significant. Furthermore, the *p*-value of <0.0001 and the agreement of adj. R^2 (0.9148) and R^2 (0.9559) values with the reduced C.V. value of 8.34% showed that the model is highly significant, while the lack of a fit test showed good predictability. In the case of A, B, AB, AC, BC, and CD, A2, B2, C2, and D2 are significant model terms. The interactive effect of these variables in terms of response surfaces is shown in Figure 2. An ANOVA table was formed by applying design expert software for checking the AB 1 degradation rate from wastewater. If more values are insignificant, then the reduction in the model

improves the model. The level of the f-value of the lack of fit applied to the model is not significant relative to the pure error. Hence, a non-significant lack of fit is good.

Table 3. CCD with predictive values and their experimental results.

Run	A	B	C	D	Degradation (%)
1	7	70	180	12.50	70
2	4	10	300	15	42
3	13	30	180	12.50	50
4	7	30	180	7.50	76
5	7	30	180	12.50	89
6	4	50	60	15	59
7	10	10	300	10	58
8	7	7	60	12.50	55
9	4	10	60	15	32
10	10	10	60	10	51
11	10	10	300	10	62
12	10	10	60	15	43
13	10	50	300	15	56
14	10	50	60	15	58
15	7	30	160	10	87
16	10	30	180	10	58
17	7	30	60	12.50	82
18	7	30	180	7	78
19	7	30	300	12.50	63
20	7	10	420	15	46
21	4	50	180	10	50
22	4	50	60	15	70
23	7	30	300	12.50	87
24	7	30	300	12.50	86
25	10	10	60	10	89
26	4	50	80	10	49
27	1	30	300	10	34
28	4	10	60	15	30.2
29	7	30	60	12.50	60.4
30	4	10	180	15.23	41.7

Three-dimensional surfaces graphically represent the interaction between two variables while the other variables are kept constant (Figure 2). pH and oxidant concentration are very sensitive factors that influence the degradation of AB 1; their interactive effect in terms of the 3D response surface over the AB 1 degradation is given in Figure 2a. As the value of the pH increases from acidic to neutral, the degradation of the dye is increased and reaches a maximum value at neutral pH. Upon further increasing the pH of the AB 1 dye sample, the degradation rate decreased. Therefore, pH 7 is optimum for the degradation of AB 1 dye. The rate of AB 1 degradation was enhanced from 1–3 mmol of oxidant concentration, and upon the further addition of oxidant concentration, the degradation rate decreased.
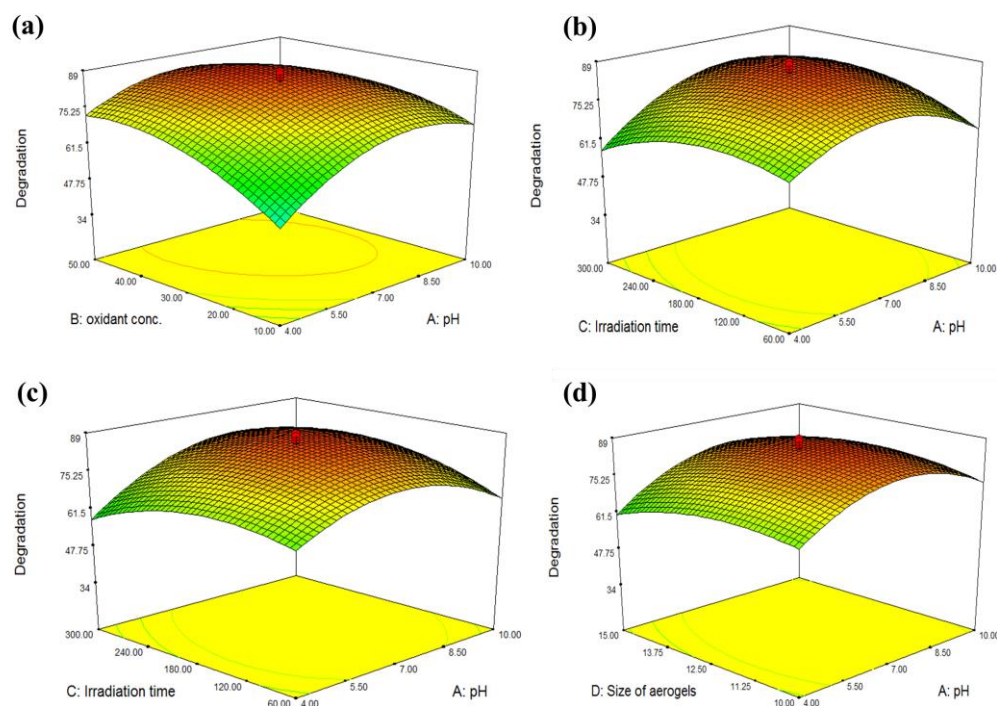
Figure 2. Interactive effects of different parameters in terms of 3D RSM plots, effect of pH and oxidant concentration (**a**), the effect of pH and irradiation time (**b**), the effect of oxidant concentration and irradiation time (**c**), and the effect of pH and the size of aerogels on the photocatalytic degradation of AB 1 dye (**d**).

The interactive effect of irradiation time and pH also influences the rate of AB 1 degradation (Figure 2b). An increase in irradiation time along with pH increased AB 1 degradation but up to a certain limit, i.e., neutral pH and an irradiation time of 180 min (Figure 2c), after which, more time did not affect the degradation rate. The size of the aerogel has a reasonable effect on the degradation rate of the dye (Figure 2d); upon an increment in the size of the aerogel, the % degradation of AB 1 dye is increased. However, upon a further increase in the aerogel size from 12.50 mm, no prominent effect in the rate of AB 1 degradation was observed.

Hence, at the optimum aerogel size of 12.50 mm at neutral pH (7), maximum AB 1 degradation was achieved. Further increases in pH decreased the degradation rate to the extent to which the aerogel size was increased. Conclusively, according to the RSM response surfaces, the optimized parameters were pH = 7, solar irradiation time = 180 min, oxidant concentration = 1–3 mmol, and at an aerogel size of 12.50 mm, the maximum degradation of AB 1 dye was achieved. Higher or lower values than the optimized conditions led to decreases in the AB 1 degradation rate, either due to changes in the surface charge (pH effect), surface area change (size of aerogel), or the scavenging or self-decomposition of hydroxyl free radicals (effect of irradiation and oxidant) produced during photocatalysis that are responsible for AB 1 dye degradation.

3.3. Evaluation of Extent of AB 1 Dye Degradation by Cr–Mn-Doped TiO_2@GO Aerogel

The AB 1 degradation by a Cr–Mn-doped TiO_2@GO aerogel photocatalytic membrane in the photocatalytic reactor was evaluated by comparing the UV/Vis spectra of AB 1 before and after treatment with a Cr–Mn-doped TiO_2@GO aerogel photocatalytic membrane. The extent of the degradation of AB 1 was evaluated by UV/Vis spectroscopy at 620 nm, and the reduction in the peak corresponding to AB 1 dye after treatment with Cr–Mn-doped TiO_2@GO aerogel photocatalytic membrane confirmed the efficient degradation of AB 1 dye (Figure 3a). Moreover, the AB 1 dye degradation was kinetically monitored (Figure 3b); it is quite obvious from the results that within 30 min of exposure to the Cr–Mn-doped TiO_2@GO

aerogel photocatalytic membrane, almost 50% of the dye was degraded, whereas in the case of blank (no membrane) and oxidant (no membrane), no remarkable AB 1 degradation was observed, confirming the efficient role of Cr–Mn-doped TiO_2@GO aerogel photocatalytic membrane in AB 1 degradation, with complete removal at 180 min.
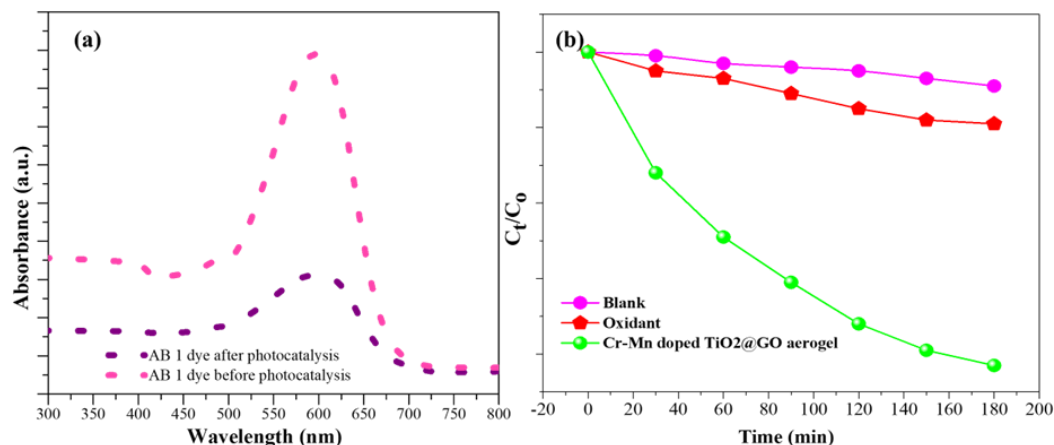

Figure 3. Evaluation of AB 1 dye degradation by UV/Vis spectrophotometer (**a**) before and after degradation using Cr–Mn-doped TiO_2@GO aerogel photocatalytic membrane. Kinetics study of AB 1 dye degradation with and without Cr–Mn-doped TiO_2@GO aerogel photocatalytic membrane (**b**).

Further, FTIR of treated and untreated AB 1 dye solution was compared. From Figure 4, it is clear that peaks corresponding to AB 1 dye clearly vanished, confirming the efficient degradation of AB 1 dye in wastewater. Peaks corresponding to stretching vibrations associated with the N-H (3200–3400 cm^{-1}), C-N (1000–1200 cm^{-1}), and N=N azo bonds (1400–1490 cm^{-1}) completely disappeared after treatment with the Cr–Mn-doped TiO_2@GO aerogel photocatalytic membrane, confirming that dye is mineralized into hydrocarbons because of the absence of other aromatics, specifically aryl amines peak (1600–1650 cm^{-1}) [56] as depicted in Figure 4.
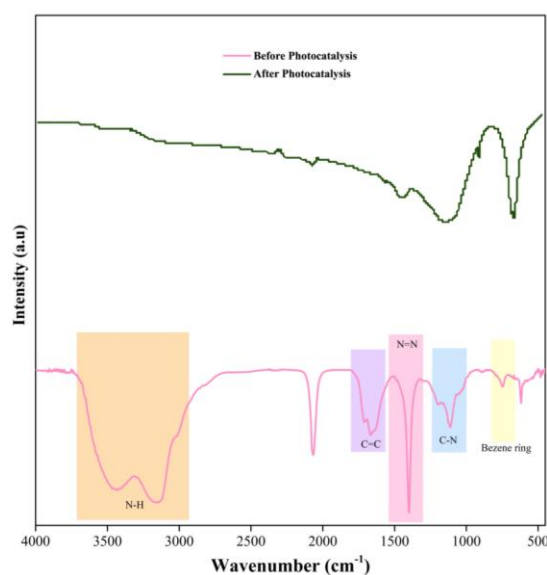

Figure 4. FTIR spectra of AB 1 dye wastewater before and after photocatalytic treatment with Cr–Mn-doped TiO_2@GO aerogel photocatalytic membrane.

A quantitative assessment of the degradation of the pollutants from water quality parameters has been analyzed before and after photocatalytic treatment with a Cr–Mn-

doped TiO$_2$@GO aerogel photocatalytic membrane. The % reduction in the COD, TOC, and BOD in wastewater has been measured. From Figure 5, it can be seen that COD is ~71%, BOD ~79%, and TOC ~61% reduced, confirming the high efficiency of the prepared Cr–Mn-doped TiO$_2$@GO aerogel photocatalytic membrane.

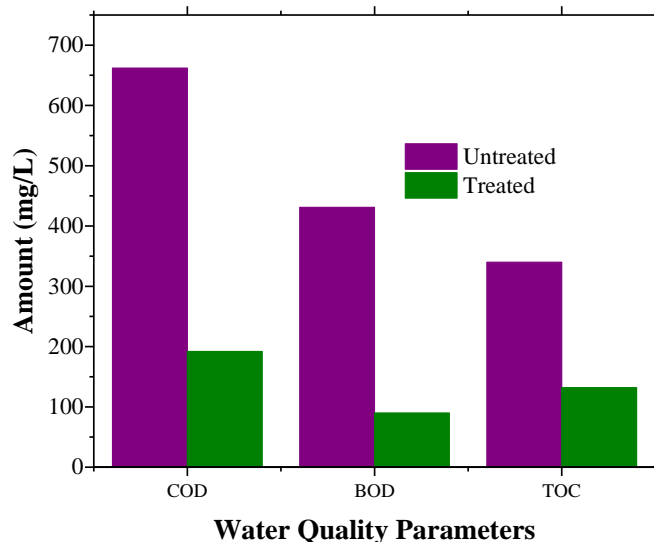**Figure 5.** Water quality parameters evaluated before and after with Cr–Mn-doped TiO$_2$@GO aerogel photocatalytic membrane.

3.4. Reusability of Cr–Mn-Doped TiO$_2$@GO Aerogel Photocatalytic Membrane

The Cr–Mn-doped TiO$_2$@GO aerogel photocatalytic membrane can be facilely separated from the reaction system for recycling. The photocatalyst with the remarkable potential of AB 1 degradation can be easily separated from the solution and can be reused with unvaried performance. Herein, the results showed that as the number of cycles of reusability increased, initially, the efficiency of the catalyst was retained, and then it continuously decreased. However, even after eight cycles of reuse, the catalyst retained its efficiency of dye degradation of more than 50% in wastewater (Figure 6). Here, the first cycle means that catalyst has already been used.
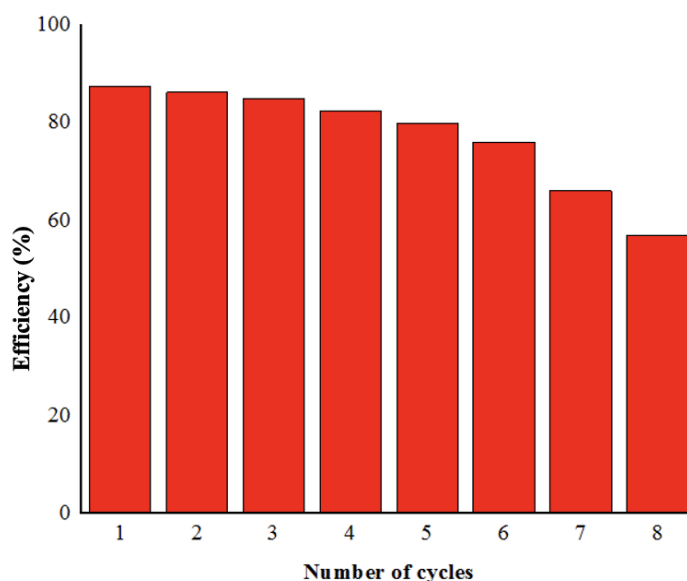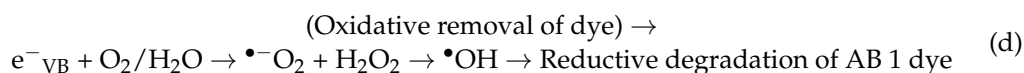

Figure 6. Reusability of the Cr–Mn-doped TiO$_2$@GO aerogel photocatalytic membrane.

3.5. Mechanism of Degradation of AB 1 Dye by Cr–Mn-Doped TiO$_2$@GO Aerogel

In the first step, (a) Cr–Mn-doped TiO$_2$@GO aerogel photocatalytic membrane, upon exposure to solar light radiation, generates an electron–hole pair (e$^-$h$^+$). h$^+$ is located in the valence band (VB) that is formed upon the excitation of e$^-$ from the VB to the conduction band (CB); the availability of both e$^-$ and h$^+$ causes the redox reaction to take place [35,57]. In the second step (b), the Cr–Mn-doped TiO$_2$@GO aerogel adsorbed the water molecules through GO functional groups. These water molecules become oxidized by the h$^+$, resulting in the formation of hydroxyl ions (OH$^-$). In the third step, (c) OH$^-$ upon further oxidation formed a hydroxyl radical ($^{\bullet}$OH), which attacks AB 1 dye, leading to its degradation into lower hydrocarbons through an oxidation reaction. Another possibility (d) of dye degradation is attributed to the presence of e$^-$ at the CB. This e$^-$ will reduce the O$_2$ molecule at the CB, resulting in the formation of $^{\bullet}$OH and superoxide anion free radicals (O$_2{}^-$), leading to the reductive degradation products of AB 1 dye.

(a) Redox reaction involved in photocatalytic degradation of AB 1 dye by Cr–Mn-doped TiO$_2$@GO aerogel photocatalytic membrane:

$$\text{Cr-Mn-doped TiO}_2\text{@GO aerogel} + h\upsilon \rightarrow \text{Cr-Mn-doped TiO}_2\text{@GO aerogel (e}^-{}_{CB} + h^+{}_{VB}) \tag{a}$$

$$h^+{}_{VB} + H_2O \rightarrow H^+ + OH^- \tag{b}$$

$$h^+{}_{VB} + OH^- \rightarrow {}^{\bullet}OH + \text{AB 1 dye} \rightarrow \text{Lower hydrocarbons} + CO_2 + H_2O + \text{Gases} \tag{c}$$

$$\text{(Oxidative removal of dye)} \rightarrow$$
$$e^-{}_{VB} + O_2/H_2O \rightarrow {}^{\bullet-}O_2 + H_2O_2 \rightarrow {}^{\bullet}OH \rightarrow \text{Reductive degradation of AB 1 dye} \tag{d}$$

(b) Overall reaction:

$$\text{Cr-Mn-doped TiO}_2\text{@GO aerogel} + {}^{\bullet}OH/{}^{\bullet-}O_2 + \text{AB 1 dye} \rightarrow \text{Oxidation/reduction products} + \text{gases}$$

Moreover, GO supports the Cr–Mn-doped TiO$_2$ and prevents charge recombination by enhancing the charge transfer to the AB 1 dye, leading to more efficient, rapid, and effective AB 1 dye degradation. Because rapid charge recombination slows down or even stops the photocatalytic activity, the presence of GO facilitates the charge separation along with the charge transfer at the surface, thus enhancing the reaction kinetics and rate of degradation of the dye. Because photocatalysis is a surface phenomenon, increased surface area leads to enhanced photocatalysis. The incorporation of GO enhanced the surface area of Cr–Mn-doped TiO$_2$. Further, $^{\bullet}$OH radical generation and the availability of active sites are proportional to the enhanced surface area. All these factors helped the Cr–Mn-doped TiO$_2$@GO aerogel photocatalytic membrane to degrade upon exposure to solar radiation.

4. Conclusions

TiO$_2$ doping is among the hot topics, due to its high catalytic performance toward the mitigation of environmental pollution; however, the band gap reduction and separation of charge holes require strategic modification by the incorporation of multiple metals. TiO$_2$ doping with Cr/Mn could reduce the band gap but has fewer adsorption capacities to selectively remove organic pollutants, especially when found in an aqueous form. GO has great potential to overcome this challenge due to its excellent absorption properties, and its conversion to an aerogel-based membrane could expose most of the reactive sites of all elements. The prepared Cr–Mn-doped TiO$_2$@GO aerogel photocatalytic membrane possesses the ability to directly absorb solar radiation to degrade dyes.

Herein, the Cr–Mn-doped TiO$_2$@GO aerogel photocatalytic membrane was successfully synthesized by the polymerization method using sodium alginate as a linker. Characterizations of the Cr–Mn-doped TiO$_2$@GO aerogel photocatalytic membrane proved it to be pure and highly crystalline, and it successfully grew over the GO nanosheets. The hydrophilic nature and higher photocatalytic properties of the Cr–Mn-doped TiO$_2$@GO aerogel photocatalytic membrane successfully degraded AB 1 dye in textile industry wastewater upon exposure to solar radiation, as confirmed by FTIR analysis, a kinetics study of

AB 1 dye degradation, and a UV–Visible spectrophotometer. Moreover, a clear ~80% reduction in COD (reduction), BOD, and TOC were observed that defines the Cr–Mn-doped TiO_2@GO aerogel photocatalytic membrane as a potential material for the economical and efficient remediation of toxic pollutants released in textile industry effluents to make that water reusable.

Author Contributions: Conceptualization, M.A. (Muhammad Ahmad), M.Y., and M.U.; methodology, M.Y., M.A. (Muhammad Ahmad) and I.A.B.; software, M.A. (Mariam Akram) and M.Y.; validation, M.A. (Muhammad Ahmad), M.U., I.A.B. and M.U.K.; formal analysis, M.Y.; investigation, M.A. (Muhammad Ahmad); resources, M.A. (Muhammad Ahmad) and M.U.; data curation, M.A. (Muhammad Ahmad) and M.Y.; writing—original draft preparation, M.Y. and M.A. (Muhammad Ahmad); writing—review and editing, M.Y., A.S., I.S., M.U.K, M.S. and M.U.; visualization, M.Y, M.U. and M.S.; supervision, M.A. (Muhammad Ahmad); project administration, M.A. (Muhammad Ahmad); funding acquisition, M.A. (Muhammad Ahmad) and I.A.B. All authors have read and agreed to the published version of the manuscript.

Institutional Review Board Statement: Not applicable.

Data Availability Statement: The data are contained within the article.

Conflicts of Interest: There are no conflict of interest to declare.

References

1. Aslam, M.M.; Kuo, H.-W.; Den, W.; Usman, M.; Sultan, M.; Ashraf, H. Functionalized Carbon Nanotubes (CNTs) for Water and Wastewater Treatment: Preparation to Application. *Sustainability* **2021**, *13*, 5717. [CrossRef]
2. Usman, M.; Waseem, M.; Mani, N.; Andiego, G. Optimization of Soil Aquifer Treatment by Chemical Oxidation with Hydrogen Peroxide Addition. *Pollution* **2018**, *4*, 369–379.
3. Benettayeb, A.; Ghosh, S.; Usman, M.; Seihoub, F.Z.; Sohoo, I.; Chia, C.H.; Sillanpää, M. Some Well-Known Alginate and Chitosan Modifications Used in Adsorption: A Review. *Water* **2022**, *14*, 1353. [CrossRef]
4. Benettayeb, A.; Usman, M.; Tinashe, C.C.; Adam, T.; Haddou, B. A Critical Review with Emphasis on Recent Pieces of Evidence of Moringa Oleifera Biosorption in Water and Wastewater Treatment. *Environ. Sci. Pollut. Res.* **2022**, *29*, 48185–48209. [CrossRef]
5. Khan, S.U.; Farooqi, I.H.; Usman, M.; Basheer, F. Energy Efficient Rapid Removal of Arsenic in an Electrocoagulation Reactor with Hybrid Fe/Al Electrodes: Process Optimization Using CCD and Kinetic Modeling. *Water* **2020**, *12*, 2876. [CrossRef]
6. Alam, R.; Khan, S.U.; Usman, M.; Asif, M.; Farooqi, I.H. A Critical Review on Treatment of Saline Wastewater with Emphasis on Electrochemical Based Approaches. *Process Saf. Environ. Prot.* **2022**, *158*, 625–643. [CrossRef]
7. Bai, B.; Bai, F.; Li, X.; Nie, Q.; Jia, X.; Wu, H. The Remediation Efficiency of Heavy Metal Pollutants in Water by Industrial Red Mud Particle Waste. *Environ. Technol. Innov.* **2022**, *28*, 102944. [CrossRef]
8. Shen, G.; Pan, L.; Lü, Z.; Wang, C.; Aleem, F.; Zhang, X.; Zou, J.-J. Fe-TiO_2 and Fe_2O_3 Quantum Dots Co-Loaded on MCM-41 for Removing Aqueous Rose Bengal by Combined Adsorption/Photocatalysis. *Chinese J. Catal.* **2018**, *39*, 920–928. [CrossRef]
9. Ahmad, M.; Yousaf, M.; Nasir, A.; Bhatti, I.A.; Mahmood, A.; Fang, X.; Jian, X.; Kalantar-Zadeh, K.; Mahmood, N. Porous Eleocharis@MnPE Layered Hybrid for Synergistic Adsorption and Catalytic Biodegradation of Toxic Azo Dyes from Industrial Wastewater. *Environ. Sci. Technol.* **2019**, *53*, 2161–2170. [CrossRef]
10. Pathania, D.; Thakur, M.; Mishra, A.K. Alginate-Zr (IV) Phosphate Nanocomposite Ion Exchanger: Binary Separation of Heavy Metals, Photocatalysis and Antimicrobial Activity. *J. Alloys Compd.* **2017**, *701*, 153–162. [CrossRef]
11. Almeida, E.J.R.; Corso, C.R. Decolorization and Removal of Toxicity of Textile Azo Dyes Using Fungal Biomass Pelletized. *Int. J. Environ. Sci. Technol.* **2019**, *16*, 1319–1328. [CrossRef]
12. Saeed, M.; Nadeem, R.; Yousaf, M. Removal of Industrial Pollutant (Reactive Orange 122 Dye) Using Environment-Friendly Sorbent Trapa Bispinosa's Peel and Fruit. *Int. J. Environ. Sci. Technol.* **2015**, *12*, 1223–1234. [CrossRef]
13. Chen, F.; Ma, J.; Zhu, Y.; Li, X.; Yu, H.; Sun, Y. Biodegradation Performance and Anti-Fouling Mechanism of an ICME/Electro-Biocarriers-MBR System in Livestock Wastewater (Antibiotic-Containing) Treatment. *J. Hazard. Mater.* **2022**, *426*, 128064. [CrossRef]
14. Wang, Q.; Wu, S.; Cui, D.; Zhou, H.; Wu, D.; Pan, S.; Xu, F.; Wang, Z. Co-Hydrothermal Carbonization of Organic Solid Wastes to Hydrochar as Potential Fuel: A Review. *Sci. Total Environ.* **2022**, *850*, 158034. [CrossRef] [PubMed]

15. Katheresan, V.; Kansedo, J.; Lau, S.Y. Efficiency of Various Recent Wastewater Dye Removal Methods: A Review. *J. Environ. Chem. Eng.* **2018**, *6*, 4676–4697. [CrossRef]

16. Bal, G.; Thakur, A. Distinct Approaches of Removal of Dyes from Wastewater: A Review. *Mater. Today Proc.* **2022**, *50*, 1575–1579. [CrossRef]

17. Liu, W.; Huang, F.; Liao, Y.; Zhang, J.; Ren, G.; Zhuang, Z.; Zhen, J.; Lin, Z.; Wang, C. Treatment of CrVI-Containing $Mg(OH)_2$ Nanowaste. *Angew. Chem.* **2008**, *120*, 5701–5704. [CrossRef]

18. Shabir, M.; Yasin, M.; Hussain, M.; Shafiq, I.; Akhter, P.; Nizami, A.-S.; Jeon, B.-H.; Park, Y.-K. A Review on Recent Advances in the Treatment of Dye-Polluted Wastewater. *J. Ind. Eng. Chem.* **2022**, *112*, 1–19. [CrossRef]

19. Chang, S.-H.; Wang, K.-S.; Li, H.-C.; Wey, M.-Y.; Chou, J.-D. Enhancement of Rhodamine B Removal by Low-Cost Fly Ash Sorption with Fenton Pre-Oxidation. *J. Hazard. Mater.* **2009**, *172*, 1131–1136. [CrossRef]

20. Liu, W.; Zheng, J.; Ou, X.; Liu, X.; Song, Y.; Tian, C.; Rong, W.; Shi, Z.; Dang, Z.; Lin, Z. Effective Extraction of Cr(VI) from Hazardous Gypsum Sludge via Controlling the Phase Transformation and Chromium Species. *Environ. Sci. Technol.* **2018**, *52*, 13336–13342. [CrossRef]

21. Singh, R.; Rattan, G.; Singh, M.; Manne, R.; Oberoi, S.K.; Kaur, N. Advanced Oxidation Processes for Wastewater Treatment: Perspective Through Nanomaterials. In *Environmental Science and Engineering, Proceedings of the International Conference on Chemical, Bio and Environmental Engineering, Jalandhar, India, 20–22 August 2021*; Springer: Berlin/Heidelberg, Germany, 2022; pp. 57–68.

22. Alemi, A.; Hanifehpour, Y.; Woo Joo, S.; Khandar, A.; Morsali, A.; Min, B.-K. Co-Reduction Synthesis of New $Ln_xSb_{2−x}S_3$ (Ln: Nd^{3+}, Lu^{3+}, Ho^{3+}) Nanomaterials and Investigation of Their Physical Properties. *Phys. B Condens. Matter* **2011**, *406*, 2801–2806. [CrossRef]

23. Wan, Z.; Zhang, T.; Liu, Y.; Liu, P.; Zhang, J.; Fang, L.; Sun, D. Enhancement of Desulfurization by Hydroxyl Ammonium Ionic Liquid Supported on Active Carbon. *Environ. Res.* **2022**, *213*, 113637. [CrossRef] [PubMed]

24. Wei, Z.; Liu, J.; Shangguan, W. A Review on Photocatalysis in Antibiotic Wastewater: Pollutant Degradation and Hydrogen Production. *Chinese J. Catal.* **2020**, *41*, 1440–1450. [CrossRef]

25. Zhang, Y.; Shaad, K.; Vollmer, D.; Ma, C. Treatment of Textile Wastewater Using Advanced Oxidation Processes—A Critical Review. *Water* **2021**, *13*, 3515. [CrossRef]

26. Shahab-ud-Din; Ahmad, M.Z.; Qureshi, K.; Bhatti, I.A.; Zahid, M.; Nisar, J.; Iqbal, M.; Abbas, M. Hydrothermal Synthesis of Molybdenum Trioxide, Characterization and Photocatalytic Activity. *Mater. Res. Bull.* **2018**, *100*, 120–130. [CrossRef]

27. Ahmad, M.; Yousaf, M.; Cai, W.; Zhao, Z.-P. Formulation of Heterometallic ZIF-8@Cu/Ni/ZnO@CNTs Heterostructure Photocatalyst for Ultra-Deep Desulphurization of Coal and Fuels. *Chem. Eng. J.* **2023**, *453*, 139846. [CrossRef]

28. Yousaf, M.; Ahmad, M.; Zhao, Z.-P. Rapid and Highly Selective Conversion of CO_2 to Methanol by Heterometallic Porous ZIF-8. *J. CO_2 Util.* **2022**, *64*, 102172. [CrossRef]

29. Liu, P.; Li, S.; Zhang, L.; Yin, X.; Ma, Y. Shearing Bridge Bonds in Carbon Nitride Vesicles with Enhanced Hot Carrier Utilization for Photocatalytic Hydrogen Production. *Catal. Sci. Technol.* **2022**, *12*, 4193–4200. [CrossRef]

30. Feng, C.; Chen, Z.; Li, W.; Zhang, F.; Li, X.; Xu, L.; Sun, M. First-Principle Calculation of the Electronic Structures and Optical Properties of the Metallic and Nonmetallic Elements-Doped ZnO on the Basis of Photocatalysis. *Phys. B Condens. Matter* **2019**, *555*, 53–60. [CrossRef]

31. Miklos, D.B.; Remy, C.; Jekel, M.; Linden, K.G.; Drewes, J.E.; Hübner, U. Evaluation of Advanced Oxidation Processes for Water and Wastewater Treatment—A Critical Review. *Water Res.* **2018**, *139*, 118–131. [CrossRef]

32. Humayun, M.; Raziq, F.; Khan, A.; Luo, W. Modification Strategies of TiO_2 for Potential Applications in Photocatalysis: A Critical Review. *Green Chem. Lett. Rev.* **2018**, *11*, 86–102. [CrossRef]

33. Li, G.; Zou, B.; Feng, S.; Shi, H.; Liao, K.; Wang, Y.; Wang, W.; Zhang, G. Synthesis of N-Doped TiO_2 with Good Photocatalytic Property. *Phys. B Condens. Matter* **2020**, *588*, 412184. [CrossRef]

34. Serga, V.; Burve, R.; Krumina, A.; Pankratova, V.; Popov, A.I.; Pankratov, V. Study of Phase Composition, Photocatalytic Activity, and Photoluminescence of TiO_2 with Eu Additive Produced by the Extraction-Pyrolytic Method. *J. Mater. Res. Technol.* **2021**, *13*, 2350–2360. [CrossRef]

35. Ajmal, A.; Majeed, I.; Malik, R.N.; Idriss, H.; Nadeem, M.A. Principles and Mechanisms of Photocatalytic Dye Degradation on TiO_2 Based Photocatalysts: A Comparative Overview. *RSC Adv.* **2014**, *4*, 37003–37026. [CrossRef]

36. Tian, B.; Li, C.; Zhang, J. One-Step Preparation, Characterization and Visible-Light Photocatalytic Activity of Cr-Doped TiO_2 with Anatase and Rutile Bicrystalline Phases. *Chem. Eng. J.* **2012**, *191*, 402–409. [CrossRef]

37. Thirupathi, B.; Smirniotis, P.G. Co-Doping a Metal (Cr, Fe, Co, Ni, Cu, Zn, Ce, and Zr) on Mn/TiO_2 Catalyst and Its Effect on the Selective Reduction of NO with NH_3 at Low-Temperatures. *Appl. Catal. B Environ.* **2011**, *110*, 195–206. [CrossRef]

38. Serga, V.; Burve, R.; Krumina, A.; Romanova, M.; Kotomin, E.A.; Popov, A.I. Extraction–Pyrolytic Method for TiO_2 Polymorphs Production. *Crystals* **2021**, *11*, 431. [CrossRef]

39. Tsebriienko, T.; Popov, A.I. Effect of Poly(Titanium Oxide) on the Viscoelastic and Thermophysical Properties of Interpenetrating Polymer Networks. *Crystals* **2021**, *11*, 794. [CrossRef]

40. Khan, I.; Chu, X.; Liu, Y.; Khan, S.; Bai, L.; Jing, L. Synthesis of Ni^{2+} Cation Modified TS-1 Molecular Sieve Nanosheets as Effective Photocatalysts for Alcohol Oxidation and Pollutant Degradation. *Chinese J. Catal.* **2020**, *41*, 1589–1602. [CrossRef]

41. Kuilla, T.; Bhadra, S.; Yao, D.; Kim, N.H.; Bose, S.; Lee, J.H. Recent Advances in Graphene Based Polymer Composites. *Prog. Polym. Sci.* **2010**, *35*, 1350–1375. [CrossRef]

42. Geim, A.K.; Novoselov, K.S. The Rise of Graphene. *Nat. Mater.* **2007**, *6*, 183–191. [CrossRef] [PubMed]

43. Zhang, J.; Qi, L.; Ran, J.; Yu, J.; Qiao, S.Z. Ternary NiS/ZnxCd1-XS/Reduced Graphene Oxide Nanocomposites for Enhanced Solar Photocatalytic H2-Production Activity. *Adv. Energy Mater.* **2014**, *4*, 1301925. [CrossRef]

44. Wu, R.; Tan, Y.; Meng, F.; Zhang, Y.; Huang, Y.-X. PVDF/MAF-4 Composite Membrane for High Flux and Scaling-Resistant Membrane Distillation. *Desalination* **2022**, *540*, 116013. [CrossRef]

45. Tan, Z.; Dong, B.; Xing, M.; Sun, X.; Xi, B.; Dai, W.; He, C.; Luo, Y.; Huang, Y. Electric Field Applications Enhance the Electron Transfer Capacity of Dissolved Organic Matter in Sludge Compost. *Environ. Technol.* **2022**, 1–11. [CrossRef]

46. Ge, D.; Yuan, H.; Xiao, J.; Zhu, N. Insight into the Enhanced Sludge Dewaterability by Tannic Acid Conditioning and PH Regulation. *Sci. Total Environ.* **2019**, *679*, 298–306. [CrossRef] [PubMed]

47. Lin, X.; Lu, K.; Hardison, A.K.; Liu, Z.; Xu, X.; Gao, D.; Gong, J.; Gardner, W.S. Membrane Inlet Mass Spectrometry Method (REOX/MIMS) to Measure 15N-Nitrate in Isotope-Enrichment Experiments. *Ecol. Indic.* **2021**, *126*, 107639. [CrossRef]

48. Dong, Y.; Shao, J.; Chen, C.; Li, H.; Wang, R.; Chi, Y.; Lin, X.; Chen, G. Blue Luminescent Graphene Quantum Dots and Graphene Oxide Prepared by Tuning the Carbonization Degree of Citric Acid. *Carbon N. Y.* **2012**, *50*, 4738–4743. [CrossRef]

49. Liu, B.; Chen, H.M.; Liu, C.; Andrews, S.C.; Hahn, C.; Yang, P. Large-Scale Synthesis of Transition-Metal-Doped TiO_2 Nanowires with Controllable Overpotential. *J. Am. Chem. Soc.* **2013**, *135*, 9995–9998. [CrossRef]

50. Zhang, H.; Ran, X.; Wu, X.; Zhang, D. Evaluation of Electro-Oxidation of Biologically Treated Landfill Leachate Using Response Surface Methodology. *J. Hazard. Mater.* **2011**, *188*, 261–268. [CrossRef]

51. El-Desoky, M.M.; Morad, I.; Wasfy, M.H.; Mansour, A.F. Synthesis, Structural and Electrical Properties of PVA/TiO_2 Nanocomposite Films with Different TiO_2 Phases Prepared by Sol–Gel Technique. *J. Mater. Sci. Mater. Electron.* **2020**, *31*, 17574–17584. [CrossRef]

52. Yasin, G.; Arif, M.; Shakeel, M.; Dun, Y.; Zuo, Y.; Khan, W.Q.; Tang, Y.; Khan, A.; Nadeem, M. Exploring the Nickel–Graphene Nanocomposite Coatings for Superior Corrosion Resistance: Manipulating the Effect of Deposition Current Density on Its Morphology, Mechanical Properties, and Erosion-Corrosion Performance. *Adv. Eng. Mater.* **2018**, *20*, 1701166. [CrossRef]

53. Yousaf, M.; Ahmad, M.; Batool, A.; Zhao, Z.-P. Highly-Stable, Bifunctional, Binder-Free & Stand-Alone Photoelectrode ($Fe_xNi_{1-X}O$@a-CC) for Natural Waters Splitting into Hydrogen. *Int. J. Hydrogen Energy* **2022**, *47*, 36032–36045. [CrossRef]

54. Mohsin, M.; Bhatti, I.A.; Ashar, A.; Khan, M.W.; Farooq, M.U.; Khan, H.; Hussain, M.T.; Loomba, S.; Mohiuddin, M.; Zavabeti, A.; et al. Iron-Doped Zinc Oxide for Photocatalyzed Degradation of Humic Acid from Municipal Wastewater. *Appl. Mater. Today* **2021**, *23*, 101047. [CrossRef]

55. Tan, Z.; Zhu, H.; He, X.; Xi, B.; Tian, Y.; Sun, X.; Zhang, H.; Ouche, Q. Effect of Ventilation Quantity on Electron Transfer Capacity and Spectral Characteristics of Humic Substances during Sludge Composting. *Environ. Sci. Pollut. Res.* **2022**, *29*, 70269–70284. [CrossRef]

56. Mbarek, W.B.; Azabou, M.; Pineda, E.; Fiol, N.; Escoda, L.; Suñol, J.J.; Khitouni, M. Rapid Degradation of Azo-Dye Using Mn–Al Powders Produced by Ball-Milling. *RSC Adv.* **2017**, *7*, 12620–12628. [CrossRef]

57. Yang, J.; Chen, C.; Ji, H.; Ma, W.; Zhao, J. Mechanism of TiO_2-Assisted Photocatalytic Degradation of Dyes under Visible Irradiation: Photoelectrocatalytic Study by TiO_2-Film Electrodes. *J. Phys. Chem. B* **2005**, *109*, 21900–21907. [CrossRef]